

Article

Photocatalytic Degradation of Ciprofloxacin with Supramolecular Materials Consisting of Nitrogenous Organic Cations and Metal Salts

Chenfei Ren , Jian Li, Xingxing Zhang and Yunyin Niu * 

Green Catalysis Center, and College of Chemistry, Zhengzhou University, Zhengzhou 450001, China

* Correspondence: niuyy@zzu.edu.cn

Abstract: The design and synthesis of composite materials with new structures/properties have important practical significance for the degradation of organic pollutants in aquatic environments. On this basis, five new supramolecular materials {[L1]₂·[Cu₄I₈]}(1), {[L1]₂·[Ag₄I₈]}(2), {[L2]·[ZnBr₄]}(3), {[L3]₂·[AgI₅]}(4), {[L3]·[CdBr₃Cl]}(5) were synthesized by introducing an amino group into a series of nitrogen-containing cationic ligands (L1–L3) through the reaction of polybromomethylbenzene with 4-aminopyridine. The degradation effect of catalysts 1–5 on ciprofloxacin (CIP) under visible light was studied using their potential catalytic properties. The results showed that compounds 1 and 4 had better degradation effects compared to other compounds. Moreover, compounds 1 and 4 were proved to be excellent catalysts for the photocatalytic degradation of CIP with cyclic experiments. Through further exploration, it was found that neutral conditions and 20 mg compound dosage were more conducive to the photodegradation of CIP by the compound. Through free radical capture experiments, it was found that ·OH played a major role in the photodegradation of CIP.

Keywords: supramolecular material; photocatalytic degradation (PDT); ciprofloxacin (CIP); catalyst



Citation: Ren, C.; Li, J.; Zhang, X.; Niu, Y. Photocatalytic Degradation of Ciprofloxacin with Supramolecular Materials Consisting of Nitrogenous Organic Cations and Metal Salts. *Catalysts* **2023**, *13*, 1134. <https://doi.org/10.3390/catal13071134>

Academic Editors: Maria Laura Tummino and Rufino Navarro Yerga

Received: 14 June 2023

Revised: 17 July 2023

Accepted: 19 July 2023

Published: 21 July 2023



Copyright: © 2023 by the authors. Licensee MDPI, Basel, Switzerland. This article is an open access article distributed under the terms and conditions of the Creative Commons Attribution (CC BY) license (<https://creativecommons.org/licenses/by/4.0/>).

1. Introduction

In recent years, the abuse of antibiotics has led to a series of environmental pollution problems [1]. Antibiotics are more or less detected in waste water, sea water, and soil [2,3], which will destroy the balance of the ecosystem and even trigger a series of chain reactions in severe cases, ultimately endangering human health [4,5]. High concentrations of antibiotics have been detected in aquatic environments, which negatively affect the structure and function of natural microbial populations (such as competitive antagonism and antimetabolite activity), thereby increasing the growth of antibiotic multi-resistant bacteria/resistant genes and potentially adverse effects on human health [6]. Because of the traditional physical adsorption method, the chemical reaction method and microbial degradation method [7–10] cannot achieve ideal results in removing antibiotics from wastewater; it is necessary to find an effective method to deal with antibiotic pollution. It has been proven that photocatalytic technology can completely mineralize refractory organic pollutants into non-toxic small molecular substances [11–18]. In addition, photocatalytic technology can be carried out under relatively mild reaction conditions without causing secondary pollution issues. Therefore, it has aroused wide attention in the removal of organic pollutants in wastewater [19–26]. At present, several common quinolone antibiotics, such as Ofloxacin (OFL), Levofloxacin (LVFX), Norfloxacin (NRFX), and Ciprofloxacin (CIP) (shown in Figure 1), belong to third-generation antibiotics. Among them, CIP has been widely used due to its broad-spectrum antibacterial activity [4]. However, since most of the CIP consumed by humans or animals cannot be metabolized and can only be excreted into the external environment, overuse of CIP may disrupt the balance of the ecosystem and cause environmental pollution [9]. Therefore, it is necessary to design and synthesize novel

compound materials for efficient degradation of CIP in a water environment, which has important practical significance.

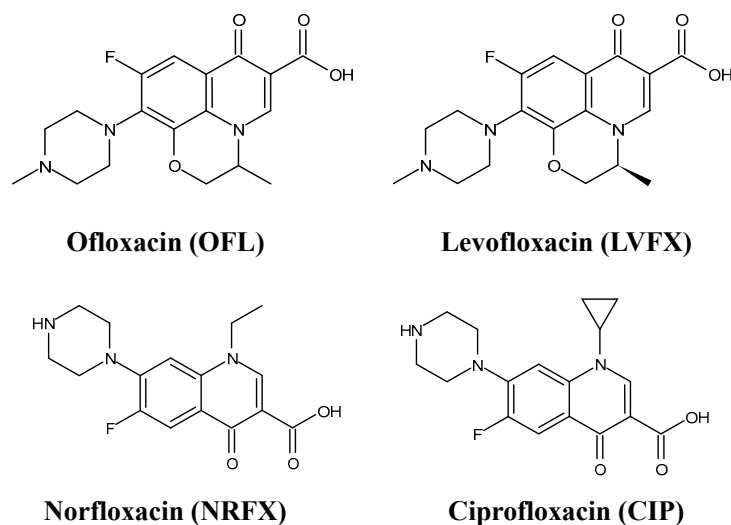


Figure 1. Structural formula of several common quinolone antibiotics.

The key of photocatalytic technology to treat target pollutants is the selection of a photocatalyst [27]. Many semiconductor materials have been studied as photocatalysts in order to better utilize solar energy. In the articles already reported, a considerable amount of research has been done to improve the performance of catalysts by modifying the original material through element doping, metal ion loading, and heterojunction construction. We envisage the selection of reactants with the goal of obtaining a target product with excellent degradation properties without modification through a one-step synthesis reaction.

Supramolecules generally refer to complex and organized functional systems formed by two or more chemical species under weak interactions (electrostatic, hydrogen bonding, π -stacking, hydrophobic and van der Waals forces, etc.), which can maintain the integrity of their own structures [28,29]. Supramolecular compounds are capable of undergoing various non-covalent interactions, such as host–guest chemistry, controlled encapsulation, hydrophobic interactions, a variety of delivering strategies, electron affinity induced interactions, etc. The emergence of supramolecular compounds has broken through the covalent bond binding mode of traditional molecular structure, and it studies the non-covalent bond weak interactions between species [30–33]. With the proposal and gradual development of supramolecular chemistry, researchers are no longer limited to the study of coordination bonds in the field of coordination chemistry, and the weak interaction between different species has attracted extensive attention from researchers [34–38]. Since the self-assembly process is affected by many factors, researchers are still exploring how to obtain supramolecular compounds with an expected structure and function. Nowadays, more and more supramolecular compounds have been reported, and researchers begin to think about how to improve their practical use value while synthesizing new compounds. Especially in the field of photocatalysis, there have been some reports about whether supramolecular compounds can be used as photocatalysts in recent years [39–43]. For example, Zhang et al. reported that the photocatalytic supramolecular material had a good photocatalytic degradation effect on methylene blue (95.8%) and rhodamine B (93.54%); Sabina et al. prepared composites containing Zn-modified MgAl LDHs and Cu-phthalocyanine as a photosensitizer, which could remove up to 93% of β -lactamide antibiotics from water. Table 1 in reference [44] provides a clearer description of the photocatalytic degradation of pollutants with supramolecular compounds.

Inorganic–organic hybrid supramolecular compounds are an important class of semiconductor materials, which are formed by the self-assembly reaction of organic molecular ligands and transition metals. The designability of organic ligands and the selectivity of

metals give them a unique structure-activity relationship. Nitrogen containing heterocyclic compounds have more aromatic rings (pyridine ring and benzene ring), which are easy to form conjugated system, and is conducive to strengthening the overall structure. In addition, these molecules contain many nitrogen atoms, which can participate in the interaction with metals or with other nitrogen atoms to easily form hydrogen bond interactions, thus further extending the structure to the three-dimensional supermolecule network.

The reaction mechanism explained by photocatalysis mainly includes three steps: light absorption, electron transfer, and reaction process. First, the photocatalyst, that is, the supramolecular compound in this work, absorbs light energy and excites electrons from the ground state to the excited state to form the excited state photocatalyst. Secondly, the excited photocatalyst is in contact with an organic pollutant, and electrons are transferred from the photocatalyst to the organic pollutant molecule to form active intermediates ($\cdot\text{OH}$, h^+ , and $\cdot\text{O}_2^-$ are all active substances for CIP degradation). Finally, the active intermediate reacts with oxygen or water molecules to form harmless substances, such as CO_2 , H_2O , etc. In the photocatalytic degradation reaction, the photocatalyst, that is, the supramolecular compound in this work, plays the role of the catalyst. According to the comparison of PXRD patterns of the compounds before and after degradation in the literature [45], the structure of the compounds did not change before and after degradation. The products of photocatalytic degradation of CIP with supramolecular compounds are: carbon dioxide, water, etc. The specific degradation process was described in the literature [45].

Therefore, in this paper, divalent nitrogen-containing cationic ligands 1, 2-bis [(4-aminopyridine)-N-methylene] benzene dibromide (**L1**), 1, 3-bis [(4-aminopyridine)-N-methylene] benzene dibromide (**L2**), and 1, 4-bis [(4-aminopyridine)-N-methylene] benzene dibromide (**L3**) had been synthesized (as shown in Figure 2) and reacted with selected inorganic metal salts through room temperature evaporation. The successful preparation of compounds 1–5 has been demonstrated with single crystal X-ray diffraction, powder X-ray diffraction, infrared spectroscopy, and elemental analysis. The degradation effect of catalysts 1–5 on ciprofloxacin (CIP) under visible light was also studied. Finally, the novelty of this study is that compounds 1 and 4 have excellent catalytic degradation of CIP through cyclic experiments.

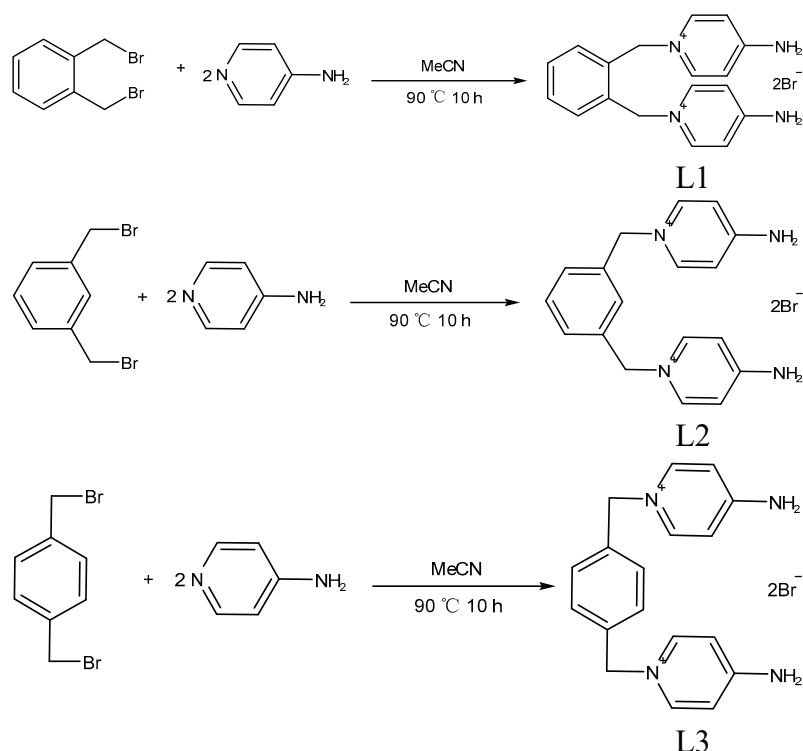


Figure 2. Reaction equation of ligands L1–L3.

2. Results and Discussion

2.1. Description of Crystal Structures of $\{[L1]_2 \cdot [Cu_4I_8]\}$ (1) and $\{[L1]_2 \cdot [Ag_4I_8]\}$ (2)

Compounds **1** and **2** are two supramolecular compounds with similar structures induced by the same nitrogen-containing organic ligand in the same way. Therefore, we focus here on compound **1**.

Compound **1** belongs to the monoclinic system and the polynomial cubane structure of the $P2_1/c$ space group. Figure 3a is the structural monomer diagram of compound **1**. It can be seen that the structural unit of compound **1** is composed of two nitrogen-containing organic ligands [L1] and an inorganic part $[Cu_4I_8]$, forming a charge-balanced supramolecular compound. In compound **1**, the inorganic part is a tetranuclear cubane structure. It can be seen from the figure that the inorganic part of compound **1** and **2** is a tetranuclear repetitive structure, and the nitrogen-containing organic ligand [L1] is regularly arranged around the inorganic cubane structure, which induces and balances the charge.

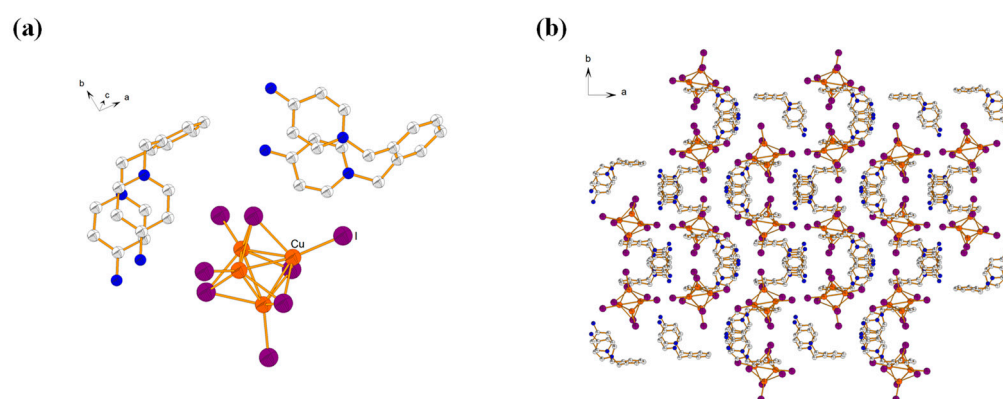


Figure 3. (a) Structural monomer diagram of compound **1**; (b) Stacking diagram of compound **1** in the c-direction.

The structure of compound **2** is very similar to that of compound **1**, in which the Ag atoms in the metal salt structure form a tetrahedron surrounded by two [L1] ligands, as shown in Figure 4a.

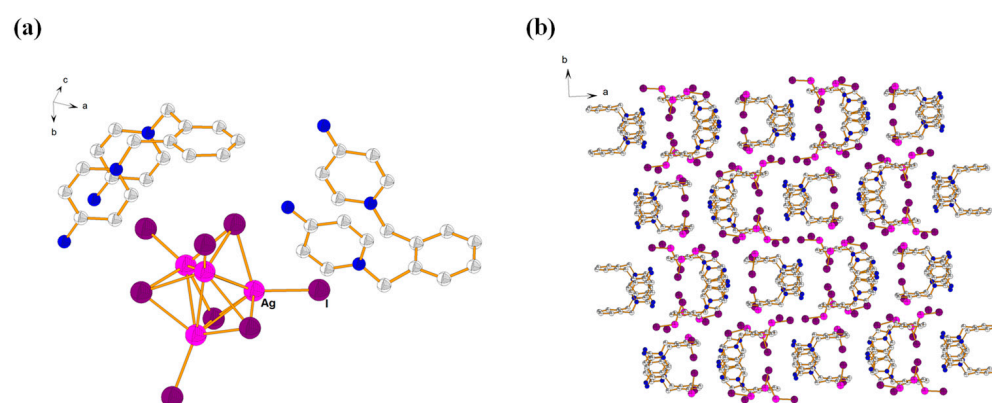


Figure 4. (a) Structural monomer diagram of compound **2**; (b) Stacking diagram of compound **2** in the c-direction.

2.2. Description of Crystal Structure of $\{[L2] \cdot [Zn(Br)_4]\}$ (3)

Compound **3** belongs to the monoclinic system and the mononuclear structure of space group $P21/c$. As shown in Figure 5a below, the asymmetric structural unit of compound **3** consists of a organic nitrogen-containing ligand [L2] and an inorganic $[Zn(Br)_4]$. Among them, the Zn atom of the inorganic part is coordinated with four Br. Figure 5b shows the stacking diagram of compound **3**, from which we can see that the inorganic part

$[\text{Zn}(\text{Br})_4]$ is regularly arranged around the nitrogen-containing organic ligand $[\text{L2}]$ to form a charge-balanced supramolecular compound.

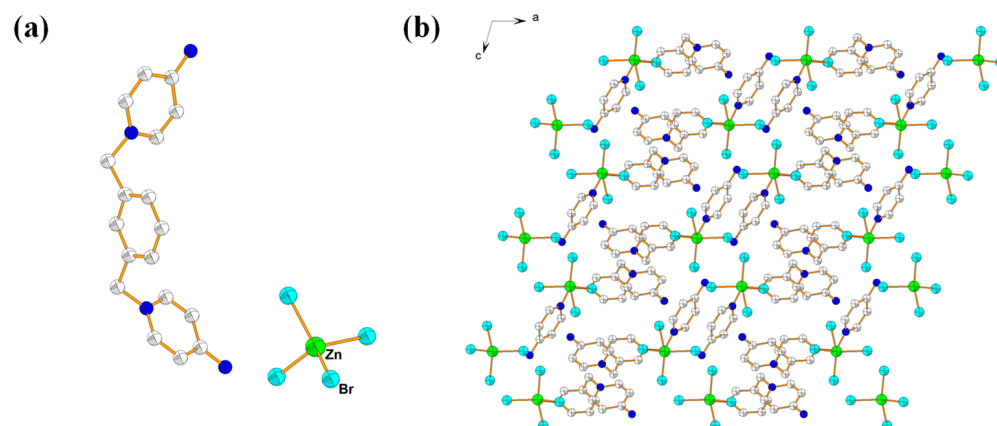


Figure 5. (a) Structural monomer diagram of compound 3; (b) Stacking diagram of compound 3 in the b-direction.

2.3. Description of Crystal Structure of $\{[\text{L3}]_2 \cdot [\text{AgI}_5]\}$ (4)

Compound 4 is a mononuclear structure of triclinic system and P-1 space group. As shown in Figure 6a, the structural unit of compound 4 contains two half $[\text{L3}]$ organic ligand and one complete $[\text{L3}]$ organic ligand, the inorganic part consists of $[\text{AgI}_4]$ and a free I. Among them, the partial Ag atom of inorganic part $[\text{AgI}_4]$ is in a tetrad coordination mode, and Figure 6b shows the accumulation structure of compound 4. It can be seen from the figure that the inorganic part of compound 4 is a mononuclear repetitive structure, around which organics are arranged regularly, forming a charge-balanced supramolecular compound.

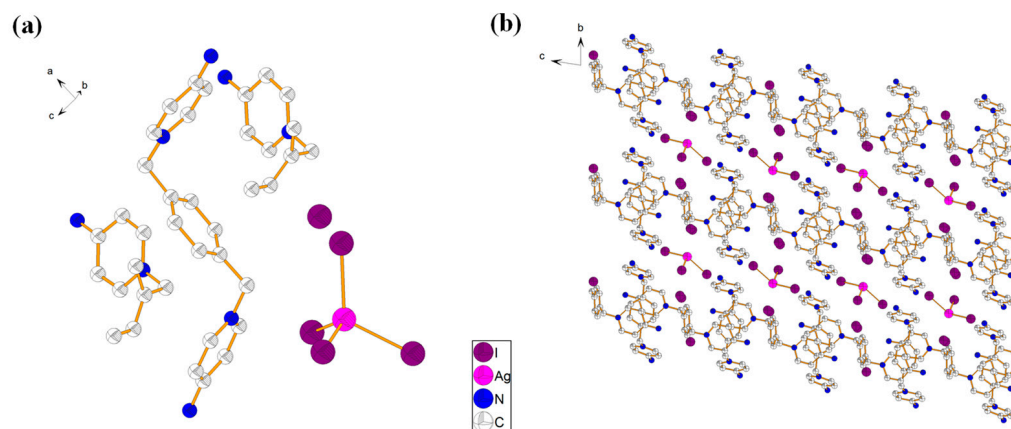


Figure 6. (a) Asymmetric structural units of compound 4; (b) Stacking diagram of compound 4 in the a-direction.

2.4. Description of Crystal Structure of $\{[\text{L3}] \cdot [\text{CdBr}_3\text{Cl}]\}$ (5)

Compound 5 belongs to the triclinic system and the mononuclear structure of P-1 space group. As shown in Figure 7a, the structural unit of compound 5 contains two halves of $[\text{L3}]$ organic and inorganic parts $[\text{CdClBr}_3]$. Among them, the inorganic $[\text{CdClBr}_3]$ partial cadmium metal is in a tetrad coordination mode, and Figure 7b shows the accumulation structure of compound 5. It can be seen that the inorganic part of compound 5 is a mononuclear repeating structure, around which organics are arranged regularly, forming a charge-balanced supramolecular compound.

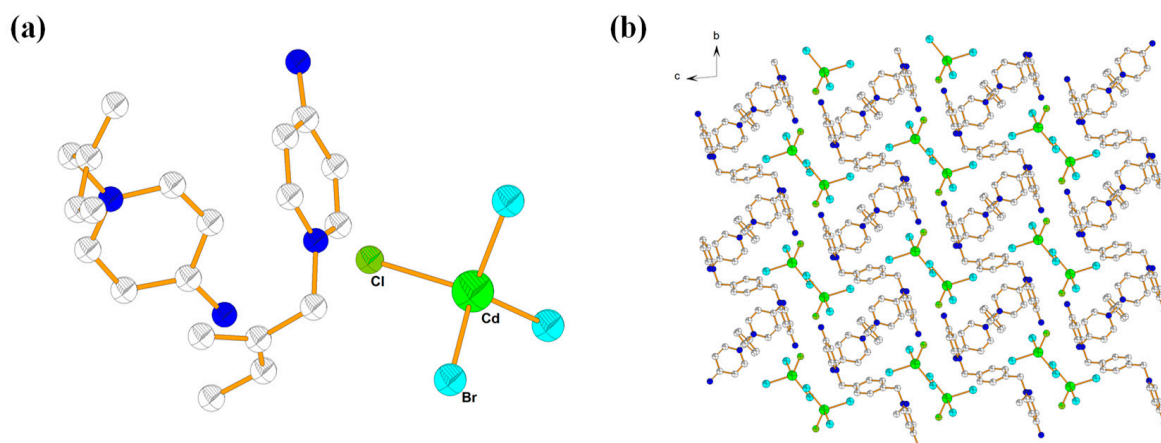


Figure 7. (a) Asymmetric structural units of compound 5; (b) Stacking diagram of compound 5 in the a-direction.

2.5. Photocatalytic Activities of Compounds 1–5

2.5.1. Semiconductor Properties of Compounds 1–5

To explore the conductivity of compounds 1–5, the UV-Vis diffuse reflectance spectra of them were measured to achieve their band gaps (E_g). The band gaps (E_g) was determined as the intersection point between the energy axis and the line extrapolated from the linear portion of the absorption edge in a plot of Kubelka–Munk function F against energy E . The Kubelka–Munk function was converted from the recorded diffuse reflectance data, where R was the reflectance of an infinitely thick layer at a given wavelength. The F versus E plot is shown in Figure 8. The Equation(1) [46,47] is as follows:

$$F = (1 - R)^2 / 2R \quad (1)$$

The band gap energy values, E_g , of compounds 1–5 are 2.01, 1.73, 2.03, 1.76, and 2.25 eV, respectively. All of them have a band gap around 2.0 eV at room temperature and belong to wide-band gap semiconductors. From physics, the wider the band gap, the more stable its physical and chemical properties, the better its radiation resistance, and the longer its life, whereas their band gap values are smaller than that of the classical inorganic photocatalyst TiO_2 (3.0–3.3 eV). This suitable band gap enables them to fully absorb sunlight, have appropriate conduction and valence band positions, and make the photogenerated carrier have enough REDOX capacity. The catalyst also has enough stability under photocatalytic reaction conditions, and its preparation and use are environmentally friendly and low-cost.

2.5.2. Degradation of CIP by Compounds 1–5

The photodegradation of CIP using compounds 1–5 as photocatalysts has been studied; 10 mg of the compound was added to the CIP solution (20 mL, $20 \text{ mg} \cdot \text{L}^{-1}$, pH = 7), and the system was transferred to a photochemical reactor (HANUO-IV, DALUO YIQI, shanghai, China). The reaction system was stirred in darkness for 30 min before light exposure to eliminate the effect of adsorption [48,49]. Then, the photocatalytic performance was tested under visible light irradiation. During the visible light irradiation, the absorbance of the solution was measured with a UV-visible spectrophotometer (UV-VIS-NIR cary5000, Agilent, Santa Clara, CA, USA). The effect of photodegradation on the CIP for compounds 1–5 is shown in Figure 9. It can be seen from the figure that compounds 1–5 have a photocatalytic degradation of CIP. Compounds 1 and 4 have better CIP degradation than the other compounds. A possible reason comes from their appropriate band gap values. Band gap values that are too large or too small are not conducive to photocatalysis.

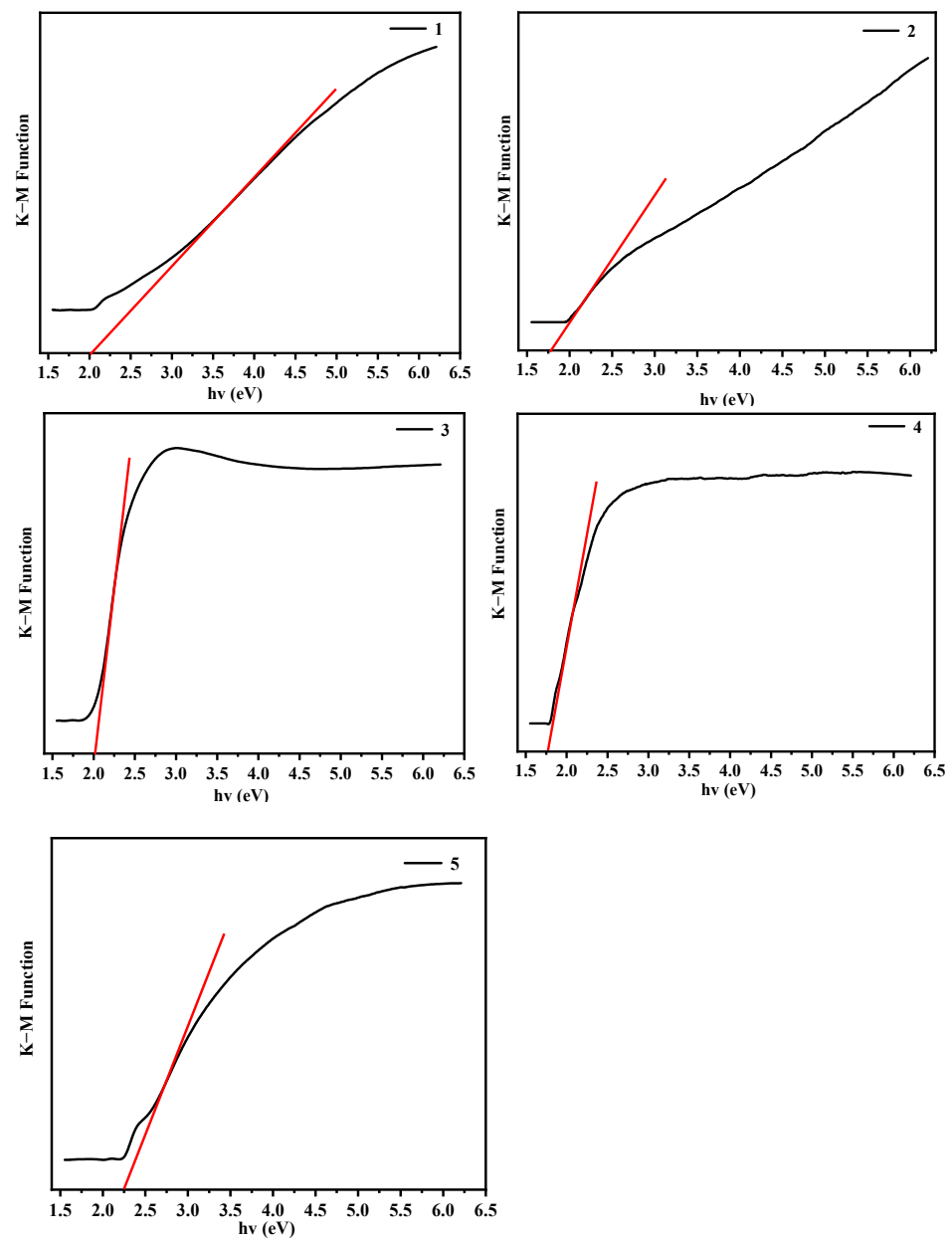


Figure 8. Band gap energy diagram of compounds 1–5.

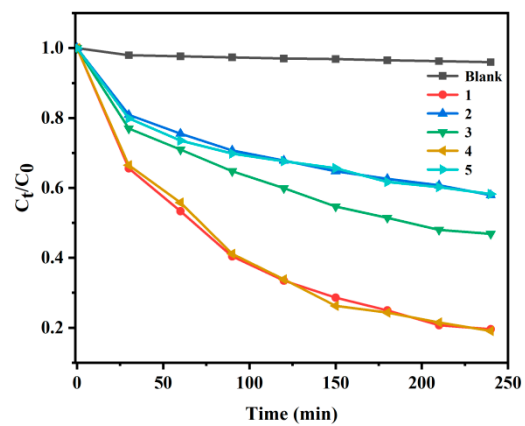


Figure 9. Rate chart of photocatalytic degradation of CIP by compounds 1–5.

2.5.3. Effect of Dosage and pH Value on Photocatalytic Effect

In order to better understand the photocatalytic process, the effects of the compound dosage and the initial pH of the solution were investigated in the case of compound 1 (Figure 10). In the compound/CIP reaction system, when the compound dosage increased from 5 mg to 20 mg, the degradation efficiency of the compound to CIP was always increased, possibly because with the increase of the compound dosage, the collision probability of the active substance and CIP also increased. Subsequently, the dosage was further increased to 30 mg and the degradation rate of CIP was found to decrease. The possible cause of this phenomenon is that the accumulation of excess compound particles clogs up and inhibits the scattering and transmission of light in the solution, reducing the rate of light utilization. In addition, the influence of the initial pH value of the solution on the photocatalytic effect was investigated, and it was found that the CIP degradation effect was the best under neutral conditions.

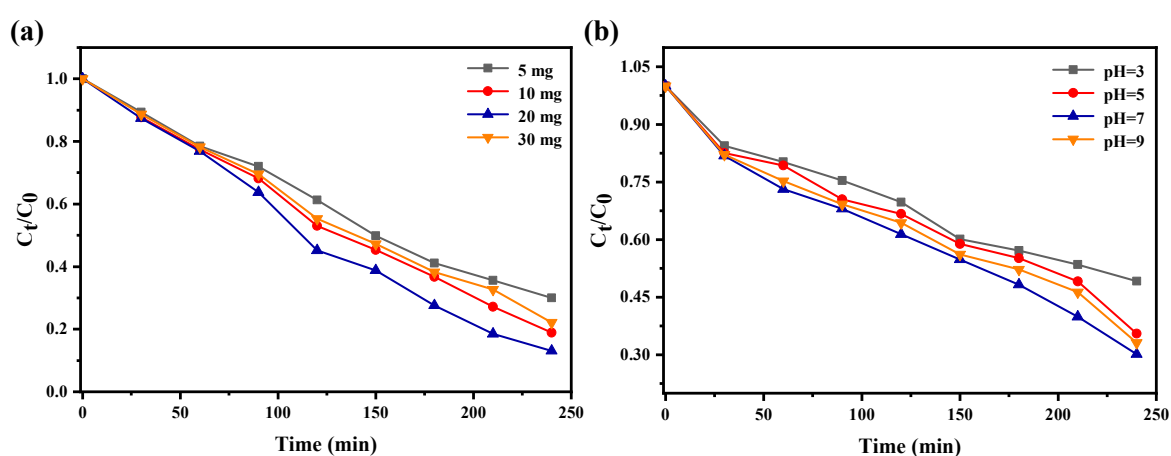


Figure 10. (a) Degradation effect of compound 1 on CIP at different dosages; (b) Degradation effect chart of compound 1 on CIP under different pH values.

2.5.4. Degradation of CIP by Compounds 1–5

In order to further study the internal mechanism of CIP degradation by compounds and to understand the active free radicals that play a major role in the catalytic degradation of CIP, active substance capture experiments were conducted. Under the same experimental conditions, different free radical scavenger was added to compound/CIP reaction system, respectively [50]. The degradation rate can be calculated by the formula:

$$\text{Removal rate} = (c_0 - c/c_0) \times 100\% \quad (2)$$

where c_0 is the concentration of degradation solution before light, and c is the concentration after degradation.

As can be seen from Figure 11, the photodegradation efficiency of CIP decreases to a certain extent when three trapping agents are added to the system, indicating that $\cdot\text{OH}$, h^+ , and $\cdot\text{O}_2^-$ are all active substances for CIP degradation. When IPA was added, the inhibition effect was most obvious, indicating that $\cdot\text{OH}$ was the main active substance involved in the photodegradation of CIP catalyzed by the compound, and h^+ and $\cdot\text{O}_2^-$ acted synergically.

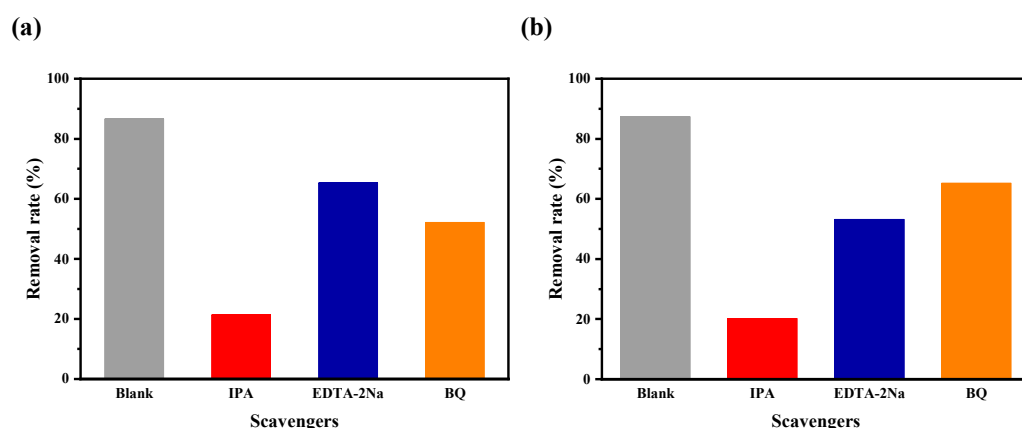


Figure 11. Effects of different free radical scavengers on the removal of CIP from compounds 1 (a) and 4 (b).

The photocatalytic stability of compounds 1 and 4 is shown in Figure 12. After each photocatalytic degradation of CIP solution, the collected compounds were washed several times with deionized water to wash the remaining CIP on the compound surface. The collected compounds were then reintroduced into fresh CIP solution to begin a new experiment. In the loop experiment, all experimental conditions and operations are the same as in the first experiment. The stability and reusability of compounds 1 and 4 in the degradation of CIP were studied through three continuous cycle experiments. As shown in Figure 12, the degradation efficiency of CIP by this compound did not decrease significantly, and the removal rate of CIP remained above 83% after three cycles of experiments. The results showed that compounds 1 and 4 could be used as stable photocatalysts for the photocatalytic degradation of CIP.

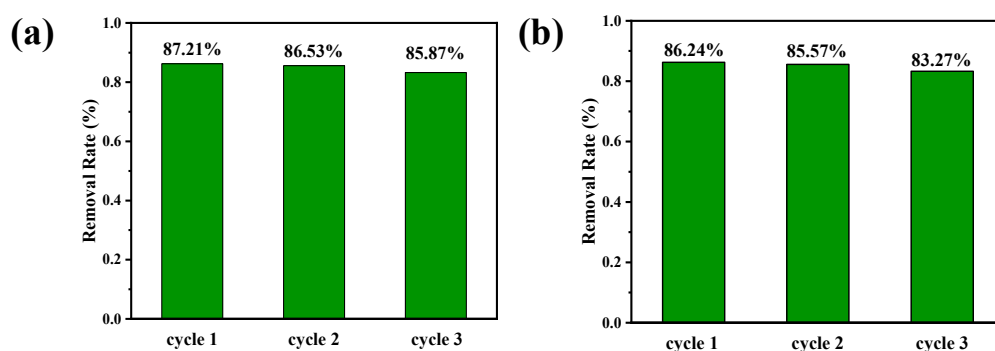


Figure 12. Removal rate of CIP by compounds 1 (a) and 4 (b) in three cycle experiments.

3. Materials and Methods

3.1. Materials

Ligands **L1**–**L3** were synthesized according to the literature [51]. The reactants were dissolved in equal amounts of acetonitrile, mixed and stirred, heated to 90 °C, and refluxed for 10 h, as shown in Figure 2.

3.2. Synthesis of Compounds

3.2.1. The Synthesis of {[L1]₂·[Cu₄I₈]} (1)

Ligand **L1**·Br₂ (0.0045 g, 0.01 mmol) was dissolved with 3 mL methanol, and appropriate amount of KI was added into the vial placed with CuI (0.0019 g, 0.01 mmol), and 3 mL acetonitrile was added into it. Dissolved ligand **L1**·Br₂ was slowly poured into CuI solution. After one week, colorless massive crystals precipitated at the bottom of the bottle. After filtration, washing, and dry collection, the yield of crystal was about 75%: IR (KBr, cm⁻¹): 3403.38 (m), 3320.05 (m), 3194.32 (m), 3040.25 (w), 1620.99 (m), 1559.03 (m),

1533.55 (m), 1511.20 (w), 1457.39 (w), 1371.40 (w), 1205.06 (w), 1166.11 (m), 1150.41 (w), 850.52 (w), 837.72 (w), 801.63 (w), 743.62 (w). Element analysis was calculated according to $C_{36}H_{40}Cu_4I_8N_8$ (1854.12): C, 23.30; H, 2.16; N, 6.04%. The actual measured value was: C, 23.25; H, 2.24; N, 6.13%.

3.2.2. The Synthesis of $\{[L1]_2 \cdot [Ag_4I_8]\}$ (2)

The synthesis of compound **2** is similar to that of compound **1** except that AgI is substituted for CuI. After about two weeks, colorless massive crystals precipitated at the bottom of the bottle. After filtration, washing, and dry collection, there was yield of about 60%: IR (KBr, cm^{-1}): 3194.57 (m), 2925.14 (w), 1650.44 (m), 1533.60 (m), 1459.16 (w), 1400.26 (w), 1205.36 (w), 1166.35 (w), 1123.15 (w), 836.45 (w), 741.18 (w), 484.38 (m). Element analysis was calculated according to $C_{36}H_{40}Ag_4I_8N_8$ (2031.44): C, 21.27; H, 1.97; N, 5.51%. The actual measured value was: C, 21.33; H, 1.92; N, 5.53%.

3.2.3. The Synthesis of $\{[L2] \cdot [ZnBr_4]\}$ (3)

The ligands **L2**·Br₂ (0.0045 g, 0.01 mmol) and ZnBr₂ (0.0023 g, 0.01 mmol) were prepared, respectively. The ligand was fully dissolved with 3 mL acetonitrile, which was dissolved by adding 2 drops of water to a vial containing ZnBr₂ and then adding 3 mL acetonitrile to it. The dissolved ligand **L2**·Br₂ was slowly poured into the acetonitrile solution of ZnBr₂. About 2 weeks later, colorless massive crystals were precipitated at the bottom of the vial. After filtration, washing, and dry collection, the yield of the crystal was about 55%: IR (KBr, cm^{-1}): 3405.11 (s), 3323.05 (s), 3222.13 (s), 3055.45 (m), 1647.55 (vs), 1619.53 (m), 1559.01 (m), 1532.25 (s), 1506.39 (m), 1494.65 (m), 1452.34 (m), 1358.38 (m), 1212.77 (m), 1179.60 (m), 1032.72 (m), 975.97 (m), 901.14 (m), 845.05 (m), 838.45 (m), 810.80 (m), 752.58 (m), 692.73 (m), 607.86 (m), 517.95 (m), 425.49 (m). Element analysis was calculated according to $C_{18}H_{20}Br_4N_4Zn$ (677.39): C, 31.89; H, 2.95; N, 8.27%. The actual measured value was: C, 31.93; H, 2.87; N, 8.31%.

3.2.4. The Synthesis of $\{[L3]_2 \cdot [AgI_5]\}$ (4)

The synthesis of compound **4** was similar to that of compound **3** except that AgI was substituted for AgBr and **L3** was substituted for **L2**. About a week later, at the bottom of the bottle, there was a colorless massive crystal precipitation. After filtration, washing, and dry collection, the yield of crystal was about 75%: IR (KBr, cm^{-1}): 3316.71 (s), 3166.63 (s), 3041.39 (m), 2670.64 (m), 1660.61 (vs), 1558.68 (m), 1541.30 (s), 1508.27 (m), 1443.77 (m), 1422.78 (m), 1373.23 (m), 1340.10 (m), 1214.60 (m), 1169.93 (s), 1039.04 (m), 963.59 (m), 933.77 (m), 872.18 (m), 843.01 (m), 817.33 (m), 783.53 (m), 758.30 (m), 708.88 (m), 572.57 (s), 494.12 (s), 431.46 (m). Elemental analysis was calculated by $C_{36}H_{40}N_8I_5Ag$ (1326.37): C, 32.57; H, 3.02; N, 8.44%. The actual measured value was: C, 32.59; H, 3.08; N, 8.39%.

3.2.5. The Synthesis of $\{[L3] \cdot [CdBr_3Cl]\}$ (5)

The synthesis of compound **5** was similar to that of compound **3** except that AgI was substituted for CdCl₂·5H₂O. About two weeks later, colorless massive crystals were precipitated at the bottom of the vial. After filtration, washing, and dry collection, the yield of crystal was about 63%: IR (KBr, cm^{-1}): 3371.74 (s), 3306.90 (s), 3197.01 (s), 3060.70 (m), 2661.96 (m), 1652.15 (vs), 1557.92 (m), 1534.28 (vs), 1511.51 (s), 1447.87 (m), 1425.71 (m), 1375.19 (m), 1346.19 (m), 1207.06 (s), 835.99 (s), 774.64 (m), 757.78 (m), 716.49 (m), 664.40 (m), 603.78 (m), 566.75 (m), 502.30 (m). Element analysis was calculated according to $C_{18}H_{20}Br_3CdClN_4$ (679.96): C, 31.77; H, 2.94; N, 8.24%. The actual measured value was: C, 31.79; H, 2.96; N, 8.26%.

3.3. Methods for Characterizing Compounds

Infrared spectrum (IR): Medium and far infrared spectrometer (Bruker VECTOR 27, Shanghai, China) used potassium bromide pressing method; the infrared spectra of the ligand and corresponding compounds were measured in the wave number range

of 400–4000 cm^{-1} (as shown in Figure 13). Solid UV diffuse reflection spectrum: the instrument model was UV-VIS-NIR Cary5000 (UV-VIS-NIR cary5000, Agilent, Santa Clara, CA, USA). Barium sulfate was used as blank control at room temperature, and the scanning range was 200–800 nm (as shown in Figure 14). Element analysis (EA): Perkin-Elmer 240 (PerkinElmer, Shanghai, China) was used to determine the content of C, H, and N elements in the obtained compounds at room temperature. Single crystal X-ray diffraction (SXRD): the instrument model was Bruker D8 VENTURE (Bruker, Karlsruhe, Germany). A single crystal with good quality was selected under the microscope as the sample to be tested. Good quality single crystal samples were generally angular, smooth surface without cracks and did not adhere to tiny grains and powdery impurities. The structure analysis and refinement of the collected crystal data were carried out by Olex2 and other programs. The main crystallographic data parameters of the compounds are shown in Table S1 of the supplementary information. The bond lengths and angles selected for compounds 1–5 are shown in Table S2; The complete crystallography data of compounds 1–5 can be obtained free of charge from The Cambridge Crystallographic Data centre via www.ccdc.cam.ac.uk/structures with CCDC numbers of 2,264,710 (for compound 1), 2,264,709 (for compound 2), 2,264,831 (for compound 3), 2,264,735 (for compound 4), and 2,264,736 (for compound 5), respectively. Powder X-ray diffraction (PXRD): instrument model for PANalytical X'Pert PRO (XRD-6100, Shimadzu, Kyoto, Japan), the radiation source for Cu-K α rays. The purity of compound was determined by comparing the coincidence between the actual measured PXRD spectra and the theoretical simulated spectra (as shown in Figure 15). A 300 W xenon lamp was selected as the visible light source for the photodegradation of CIP with compounds 1–5.

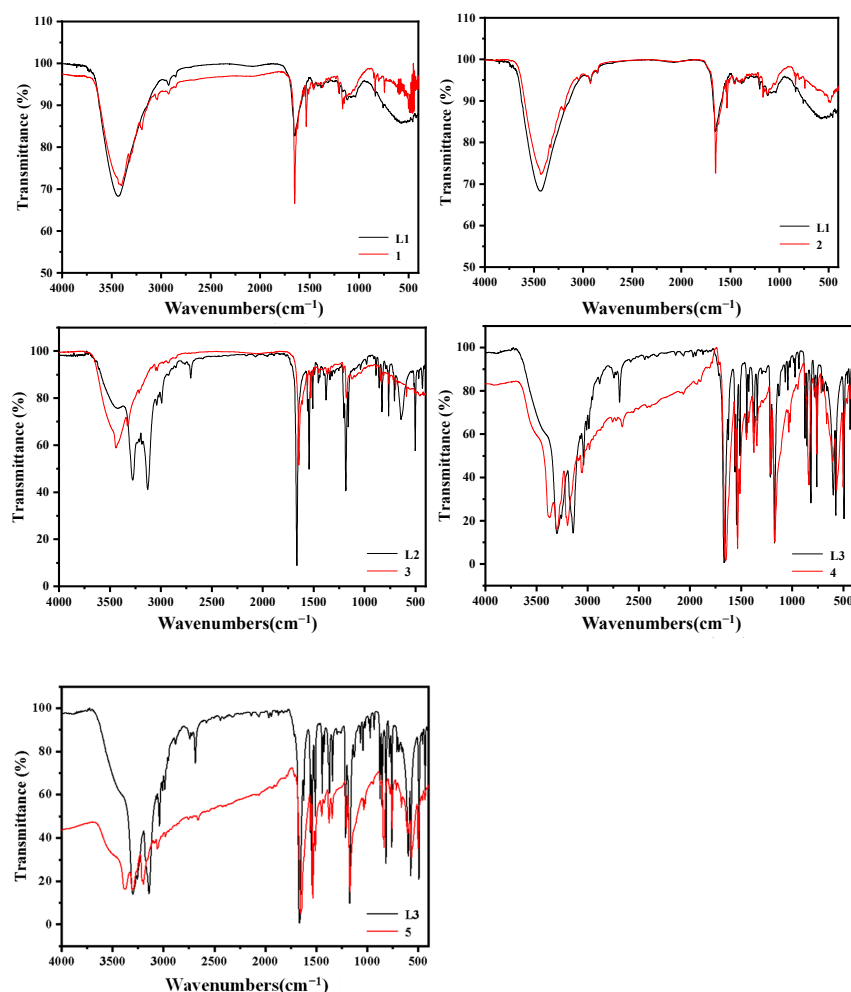


Figure 13. Infrared diagram of compounds 1–5.

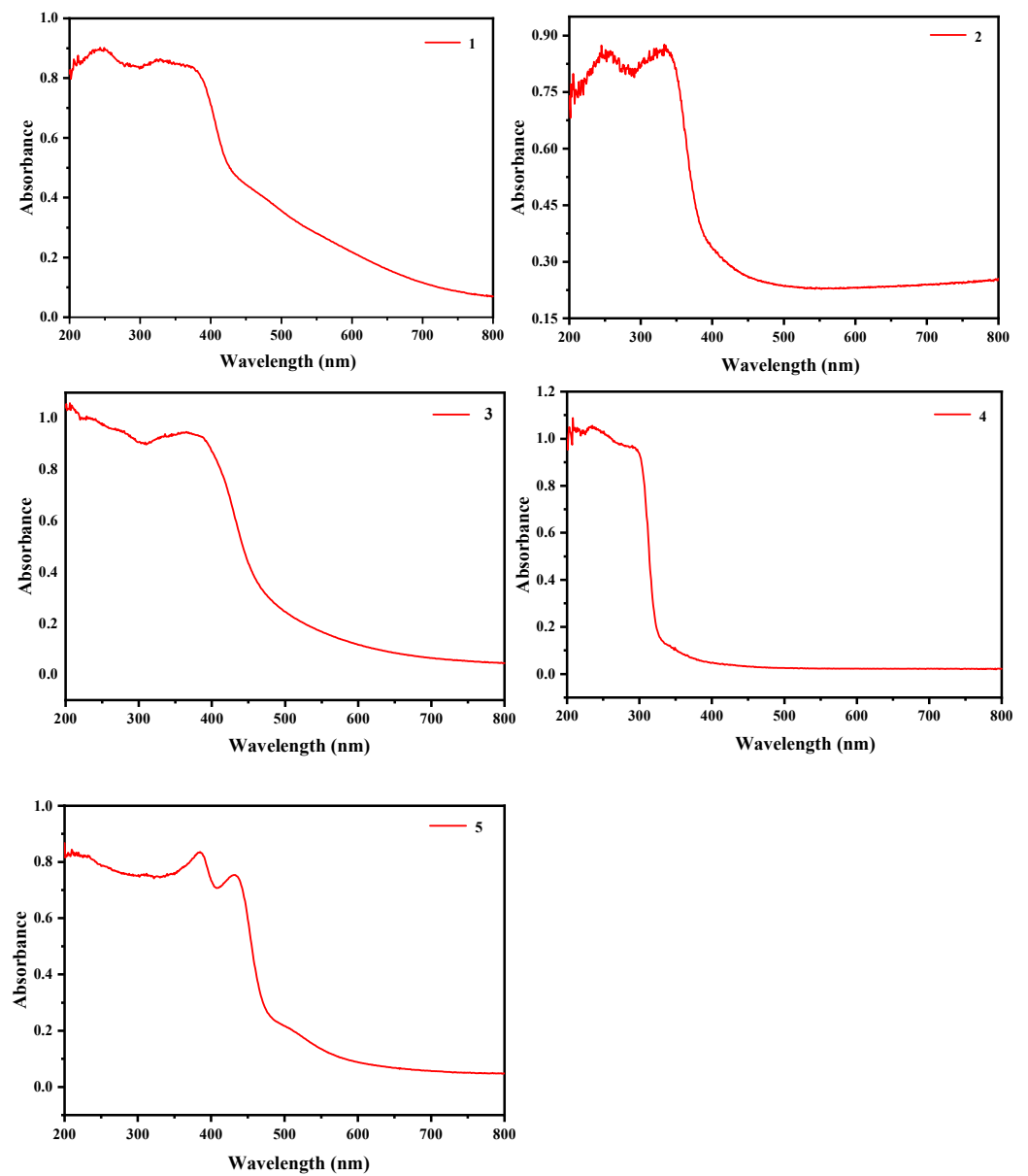


Figure 14. UV-VIS diffuse reflectance spectra of compounds 1–5.

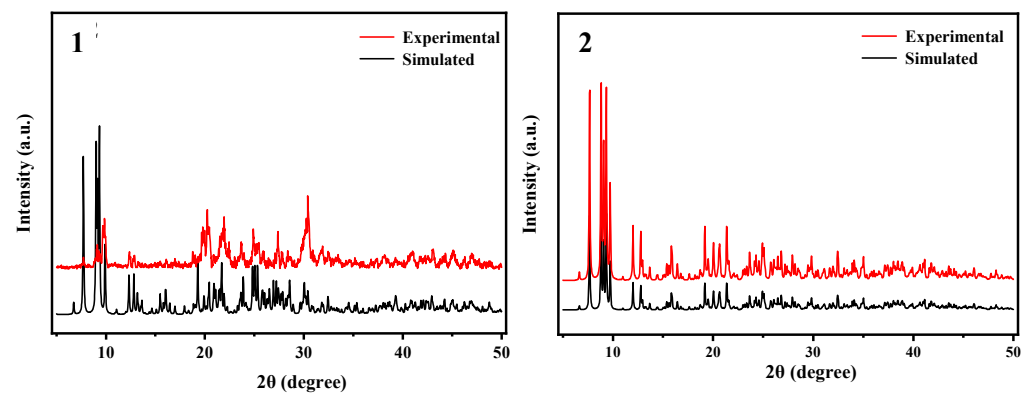


Figure 15. Cont.

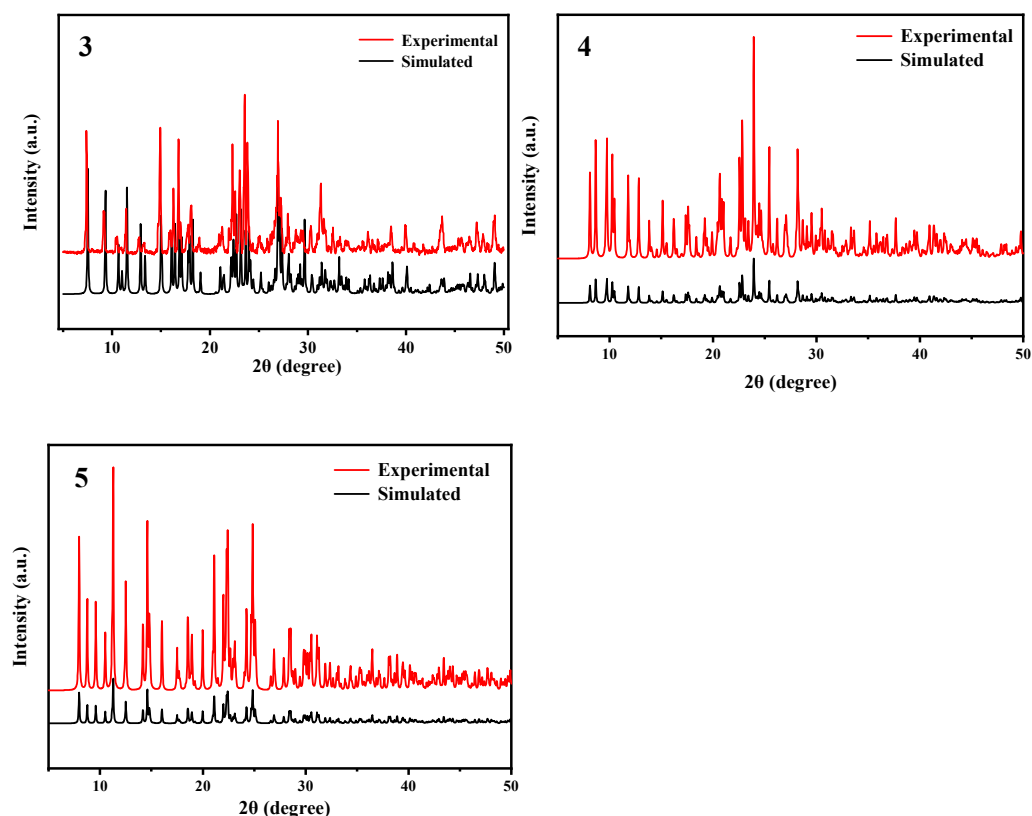


Figure 15. PXRD diagram of compounds 1–5.

4. Conclusions

In this paper, five supramolecular compounds were obtained with the reaction of ligands L1–L3 with metal salts at room temperature. Simultaneously, the successful preparation of the compounds was proven with the infrared spectrum, ultraviolet spectrum, elemental analysis, and PXRD characterization. The photodegradation performance of compounds 1–5 as photocatalysts against CIP was preliminarily investigated. Compared with other compounds, compounds 1 and 4 showed better degradation effects. Through further investigation, it was found that neutral conditions and a compound dosage of 20 mg were more conducive to CIP photodegradation. Through free radical capture experiments, it was found that $\cdot\text{OH}$ played a major role in the photodegradation of CIP. The highlight of this work is that the cyclic experiments show that compounds 1 and 4 have the best catalytic degradation performance of CIP, and the optimal dose and pH value of CIP degradation are obtained.

Supplementary Materials: The following supporting information can be downloaded at: <https://www.mdpi.com/article/10.3390/catal13071134/s1>, Table S1: Crystal data and structural refinement details of complexes 1–5, Table S2: The main bond length and bond angle of compounds 1–5.

Author Contributions: Conceptualization, C.R. and Y.N.; methodology, C.R., X.Z. and Y.N.; software, C.R.; validation, C.R., X.Z. and Y.N.; formal analysis, Y.N.; investigation, C.R., J.L. and Y.N.; resources, J.L.; data curation, C.R.; writing—original draft preparation, C.R. and Y.N.; writing—review and editing, C.R. and Y.N.; visualization, C.R. and Y.N. All authors have read and agreed to the published version of the manuscript.

Funding: This research received no external funding.

Data Availability Statement: No new data were created or analyzed in this study. Data sharing is not applicable to this article.

Acknowledgments: The authors would like to thank Professor Niu Yunyin of the College of Chemistry, Zhengzhou University for his guidance. All individuals included in this section have consented to the acknowledgement.

Conflicts of Interest: The authors declare no conflict of interest.

References

1. Rosi-Marshall, E.J.; Kincaid, D.W.; Bechtold, H.A.; Royer, T.V.; Rojas, M.; Kelly, J.J. Pharmaceuticals suppress algal growth and microbial respiration and alter bacterial communities in stream biofilms. *Ecol. Appl.* **2013**, *23*, 583–593. [[CrossRef](#)] [[PubMed](#)]
2. Qiao, M.; Ying, G.G.; Singer, A.C.; Zhu, Y.G. Review of antibiotic resistance in China and its environment. *Environ. Int.* **2018**, *110*, 160–172. [[CrossRef](#)] [[PubMed](#)]
3. Yezli, S.; Li, H. Antibiotic resistance amongst healthcare-associated pathogens in China. *Int. J. Antimicrob. Agents* **2012**, *40*, 389–397. [[CrossRef](#)] [[PubMed](#)]
4. Rodriguez-Mozaz, S.; Chamorro, S.; Marti, E.; Huerta, B.; Gros, M.; Sánchez-Melsió, A.; Borrego, C.M.; Barceló, D.; Balcázar, J.L. Occurrence of antibiotics and antibiotic resistance genes in hospital and urban wastewaters and their impact on the receiving river. *Water Res.* **2015**, *69*, 234–242. [[CrossRef](#)]
5. Tong, L.; Li, P.; Wang, Y.; Zhu, K. Analysis of veterinary antibiotic residues in swine wastewater and environmental water samples using optimized SPE-LC/MS/MS. *Chemosphere* **2009**, *74*, 1090–1097. [[CrossRef](#)]
6. Nguyen, L.T.; Nguyen, H.T.; Pham, T.D.; Tran, T.D.; Chu, H.T.; Dang, H.T.; Nguyen, V.H.; Nguyen, K.M.; Pham, T.T.; Van der Bruggen, B. UV-Visible Light Driven Photocatalytic Degradation of Ciprofloxacin by N,S Co-doped TiO₂: The Effect of Operational Parameters. *Top. Catal.* **2020**, *63*, 985–995. [[CrossRef](#)]
7. Pan, M.; Chu, L.M. Occurrence of antibiotics and antibiotic resistance genes in soils from wastewater irrigation areas in the Pearl River Delta region, southern China. *Sci. Total Environ.* **2018**, *624*, 145–152. [[CrossRef](#)]
8. Liang, Z.; Zhaob, Z.; Sun, T.; Shi, W.; Cui, F. Adsorption of quinolone antibiotics in spherical mesoporous silica: Effects of the retained template and its alkyl chain length. *J. Hazard. Mater.* **2016**, *305*, 8–14. [[CrossRef](#)]
9. Álvarez-Torrellas, S.; Peres, J.A.; Gil-Álvarez, V.; Ovejero, G.; García, J. Effective adsorption of non-biodegradable pharmaceuticals from hospital wastewater with different carbon materials. *Chem. Eng. J.* **2017**, *320*, 319–329. [[CrossRef](#)]
10. Lyu, J.; Shao, J.; Wang, Y.; Qiu, Y.; Li, J.; Li, T.; Peng, Y.; Liu, F. Construction of a porous core-shell homojunction for the photocatalytic degradation of antibiotics. *Chem. Eng. J.* **2019**, *358*, 614–620. [[CrossRef](#)]
11. Murugesan, S.; Huda, M.N.; Yan, Y.; Al-Jassim, M.M.; Subramanian, V. Band-Engineered Bismuth Titanate Pyrochlores for Visible Light Photocatalysis. *J. Phys. Chem. C* **2010**, *114*, 10598–10605. [[CrossRef](#)]
12. Yu, X.; Huang, L.; Wei, Y.; Zhang, J.; Zhao, Z.; Dai, W.; Yao, B. Controllable preparation, characterization and performance of Cu₂O thin film and photocatalytic degradation of methylene blue using response surface methodology. *Mater. Res. Bull.* **2015**, *64*, 410–417. [[CrossRef](#)]
13. Hou, X.; Cai, Y.; Mushtaq, M. Deposition of TiO₂ Nanoparticles on Porous Polylactic Acid Fibrous Substrates and Its Photocatalytic Capability. *J. Nanosci. Nanotechnol.* **2018**, *18*, 5617–5623. [[CrossRef](#)]
14. Kumar, A.; Kumar, A.; Sharma, G.; Naushad, M.; Stadler, F.J.; Ghfar, A.A.; Dhiman, P.; Saini, R.V. Sustainable nano-hybrids of magnetic biochar supported g-C₃N₄/FeVO₄ for solar powered degradation of noxious pollutants- Synergism of adsorption, photocatalysis & photo-ozonation. *J. Cleaner Prod.* **2017**, *165*, 431–451.
15. Li, Y.; Xiao, M.; Niu, Y. Preparation and application of two kinds of supramolecular compounds with photodegradation of organic contaminants in wastewater. *Main Group Chem.* **2019**, *18*, 43–54. [[CrossRef](#)]
16. Wang, F.R.; Wang, C.H.; Wu, B.L.; Yan, Z.N.; Niu, Y.Y.; Hou, H.W. Synthesis, structure and photocatalytic properties of two hybrid compounds prepared by N-methyl-4,4'-bipyridinium chloride. *Main Group Chem.* **2018**, *17*, 211–218. [[CrossRef](#)]
17. Liu, X.J.; Qiao, X.Y.; Niu, Y.Y. Synthesis, structures and properties of Cd(II) supramolecular compound based on nitrogen heterocyclic cation. *Main Group Chem.* **2020**, *19*, 199–206. [[CrossRef](#)]
18. Qiao, G.Y.; Li, S.M.; Niu, Y.Y. One new copper iodide coordination polymer directed by 4-pyridyl dithioether ligand: Syntheses, structures, and photocatalysis. *Main Group Chem.* **2020**, *19*, 217–225. [[CrossRef](#)]
19. Xing, X.; Du, Z.; Zhuang, J.; Wang, D. Removal of ciprofloxacin from water by nitrogen doped TiO₂ immobilized on glass spheres: Rapid screening of degradation products. *J. Photochem. Photobiol. A* **2018**, *359*, 23–32. [[CrossRef](#)]
20. Zhang, L.; Wong, K.H.; Chen, Z.; Yu, J.C.; Zhao, J.; Hu, C.; Chan, C.Y.; Wong, P.K. AgBr-Ag-Bi₂WO₆ nanojunction system: A novel and efficient photocatalyst with double visible-light active components. *Appl. Catal. A* **2009**, *363*, 221–229. [[CrossRef](#)]
21. Gan, Y.; Wei, Y.; Xiong, J.; Cheng, G. Impact of post-processing modes of precursor on adsorption and photocatalytic capability of mesoporous TiO₂ nanocrystallite aggregates towards ciprofloxacin removal. *Chem. Eng. J.* **2018**, *349*, 1–16. [[CrossRef](#)]
22. Yang, Y.; Banerjee, G.; Brudvig, G.W.; Kim, J.H.; Pignatello, J.J. Oxidation of Organic Compounds in Water by Unactivated Peroxymonosulfate. *Environ. Sci. Technol.* **2018**, *52*, 5911–5919. [[CrossRef](#)] [[PubMed](#)]
23. Zhang, W.; Ma, Y.; Yang, Z.; Tang, X.; Li, X.; He, G.; Cheng, Y.; Fang, Z.; He, R.; Zhang, Y. Analysis of synergistic effect between graphene and octahedral cuprous oxide in cuprous oxide-graphene composites and their photocatalytic application. *J. Alloys Compd.* **2017**, *712*, 704–713. [[CrossRef](#)]

24. Wang, X.J.; Qiao, X.Y.; Niu, Y.Y. Synthesis, characterization, adsorption and catalytic activity of a polyoxometalate supramolecule templated by arylmethylamine. *Main Group Chem.* **2020**, *19*, 187–198. [[CrossRef](#)]
25. Li, J.; Liu, Z.; Liu, Y.Y.; Liu, J.; Li, Y.Y.; Qiao, X.Y.; Huang, W.M.; Niu, Y.Y. POM-based Metal–organic Compounds: Assembly, Structures and Properties. *Main Group Chem.* **2021**, *20*, 575–592. [[CrossRef](#)]
26. Guo, X.Y.; Wang, X.J.; Liu, Z.; Liu, Y.Y.; Liu, J.; Niu, Y.Y. Two Supramolecular Compounds Constructed by Polyacid Anion Clusters: Synthesis, Characterization and Performance Research. *Main Group Chem.* **2021**, *20*, 601–610. [[CrossRef](#)]
27. Kaur, M.; Umar, A.; Mehta, S.K.; Kansal, S.K. Reduced graphene oxide–CdS heterostructure: An efficient fluorescent probe for the sensing of Ag(I) and sunset yellow and a visible-light responsive photocatalyst for the degradation of levofloxacin drug in aqueous phase. *Appl. Catal. B* **2019**, *245*, 143–158. [[CrossRef](#)]
28. Kolesnichenko, I.V.; Ansly, E.V. Practical Applications of Supramolecular Chemistry. *Chem. Soc. Rev.* **2017**, *46*, 197–238. [[CrossRef](#)]
29. Christopher, B.R.; Joshua, E.M.; Jason, A.B. Supramolecular Guest–Host Interactions for the Preparation of Biomedical Materials. *Bioconjugate Chem.* **2015**, *26*, 2279–2289.
30. Prins, L.J.; Reinhoudt, D.N.; Timmerman, P. Noncovalent Synthesis using Hydrogen Bonding. *Angew. Chem. Int. Ed.* **2001**, *40*, 2382–2426. [[CrossRef](#)]
31. Fyfe, M.C.T.; Stoddart, J.F. Synthetic Supramolecular Chemistry. *Acc. Chem. Res.* **1997**, *30*, 393–401. [[CrossRef](#)]
32. Mueller-Dethlefs, K.; Hobza, P. Noncovalent Interactions: A Challenge for Experiment and Theory. *Chem. Rev.* **2000**, *100*, 143–167. [[CrossRef](#)]
33. Hamley, I. Nanotechnology with Soft Materials. *Angew. Chem. Int. Ed.* **2003**, *42*, 1692–1712. [[CrossRef](#)]
34. Mammen, M.; Chio, S.K.; Whitesides, G.M. Polyvalent Interactions in Biological Systems: Implications for Design and Use of Multivalent Ligands and Inhibitors. *Angew. Chem. Int. Ed.* **1998**, *37*, 2755–2794. [[CrossRef](#)]
35. Ercolani, G. Assessment of Cooperativity in Self-Assembly. *J. Am. Chem. Soc.* **2003**, *125*, 16097–16103. [[CrossRef](#)]
36. Lundquist, J.J.; Toone, E.J. The Cluster Glycoside Effect. *Chem. Rev.* **2002**, *102*, 555–578. [[CrossRef](#)]
37. Kitov, P.I.; Bundle, D.R. On the Nature of the Multivalency Effect: A Thermodynamic Model. *J. Am. Chem. Soc.* **2003**, *125*, 16271–16284. [[CrossRef](#)]
38. Lee, Y.C.; Lee, R.T. Carbohydrate–Protein Interactions: Basis of Glycobiology. *Acc. Chem. Res.* **1995**, *28*, 321–327. [[CrossRef](#)]
39. Zhang, L.Y.; Zhao, X.Y.; Wang, C.M.; Yu, K.; Lv, J.H.; Wang, C.X.; Zhou, B.B. The supercapacitor and photocatalytic supermolecule materials constructed by 4′-pyridine and {PMO₁₂O₄₀}. *J. Solid State Chem.* **2022**, *312*, 123235. [[CrossRef](#)]
40. Sabina, G.I.; Octavian, D.P.; Nicolae, G.; Madalina, T.; Simona, M.C.; Vasile, I.P.; Bogdan, C.; Elisabeth, E.J. Use of Photocatalytically Active Supramolecular Organic–Inorganic Magnetic Composites as Efficient Route to Remove β -Lactam Antibiotics from Water. *Catalysts* **2022**, *12*, 1044.
41. Zhou, X.H.; Chen, Y.Y.; Wang, P.Y.; Xu, C.Y.; Yan, Q.S. Fabrication of AgI/BiPO₄ n–n heterojunction photocatalyst for efficient degradation of organic pollutants. *J. Mater. Sci. Mater. Electron.* **2020**, *31*, 12638–12648. [[CrossRef](#)]
42. Lu, J.R.; Yue, M.T.; Cui, W.Q.; Sun, C.H.; Liu, L. Supramolecular photocatalyst of perylene bisimide decorated with α -Fe₂O₃: Efficient photo-Fenton degradation of organic pollutants. *Colloids Surf. A Physicochem. Eng. Asp.* **2022**, *655*, 130222. [[CrossRef](#)]
43. Bao, S.H.; Wu, S.S.; Huang, L.P.; Xu, X.; Xu, R.; Li, Y.G.; Liang, Y.R.; Yang, M.Y.; Yoon, D.K.; Lee, M.; et al. Supramolecular Nanopumps with Chiral Recognition for Moving Organic Pollutants from Water. *ACS Appl. Mater. Interfaces* **2019**, *11*, 31220–31226. [[CrossRef](#)] [[PubMed](#)]
44. Zhang, X.X.; Wang, X.J.; Niu, Y.-Y. Photocatalytic Degradation of Tetracycline by Supramolecular Materials Constructed with Organic Cations and Silver Iodide. *Catalysts* **2022**, *12*, 1581. [[CrossRef](#)]
45. Ren, C.; Li, J.; Zhang, X.; Niu, Y. Synthesis and Photocatalytic Properties of Four Coordination Compounds Constructed from Two Benzimidazole-Based Asymmetric Polyazocyclic Ligands. *Molecules* **2023**, *28*, 3841. [[CrossRef](#)]
46. Xia, Y.; Wu, P.F.; Wei, Y.G.; Wang, Y.; Guo, H.Y. Synthesis, Crystal Structure, and Optical Properties of a Polyoxometalate-Based Inorganic–Organic Hybrid Solid, (n-Bu₄N)₂[Mo₆O₁₇(\equiv NAr)₂] (Ar = o-CH₃OC₆H₄). *Cryst. Growth Des.* **2006**, *6*, 253–257. [[CrossRef](#)]
47. Liu, H.Y.; Bo, L.; Yang, J.; Liu, Y.Y.; Ma, J.F.; Wu, H. Two novel inorganic–organic hybrid materials constructed from two kinds of octamolybdate clusters and flexible tetradentate ligands. *Dalton Trans* **2011**, *40*, 9782–8. [[CrossRef](#)]
48. Wang, J.; Yang, Z.; Gao, X.; Yao, W.; Wei, W.; Chen, X.; Zong, R.; Zhu, Y. Core-shell g-C₃N₄@ZnO composites as photoanodes with double synergistic effects for enhanced visible-light photoelectrocatalytic activities. *Appl. Catal. B* **2017**, *217*, 169–180. [[CrossRef](#)]
49. Wang, P.; Wu, T.; Wang, C.; Hou, J.; Qian, J.; Ao, Y. Combining Heterojunction Engineering with Surface Cocatalyst Modification To Synergistically Enhance the Photocatalytic Hydrogen Evolution Performance of Cadmium Sulfide Nanorods. *ACS Sustain. Chem. Eng.* **2017**, *5*, 7670–7677. [[CrossRef](#)]
50. Liang, H.; Tai, X.; Du, Z. Photocatalytic degradation of nonylphenol ethoxylate and its degradation mechanism. *J. Mol. Liq.* **2020**, *302*, 112567.
51. Xu, M.M.; Li, Y.; Zheng, L.J.; Niu, Y.Y.; Hou, H.W. Three cation-templated Cu(I) self-assemblies: Synthesis, structures, and photocatalytic properties. *New J. Chem.* **2016**, *40*, 6086–6092. [[CrossRef](#)]

Disclaimer/Publisher’s Note: The statements, opinions and data contained in all publications are solely those of the individual author(s) and contributor(s) and not of MDPI and/or the editor(s). MDPI and/or the editor(s) disclaim responsibility for any injury to people or property resulting from any ideas, methods, instructions or products referred to in the content.